International Journal of Structural Stability and Dynamics © World Scientific Publishing Company

A Small-Deformation Rate-Independent Continuous-Flow Model for Elasto-Plastic Frames Allowing Rapid Fatigue Predictions in Metallic Structures

Dominic Jarecki[†], Bensingh Dhas[†], Arun Srinivasa^{†*}, and J. N. Reddy[†]

[†]Department of Mechanical Engineering
Texas A&M University College Station, Texas 77845 USA

Received (Day Month Year) Accepted (Day Month Year)

Fatigue analysis in metallic frame structures can be challenging due to associated computational costs; if localized plasticity is involved, then the approach of three-dimensional continuum plasticity models for direct computation of stresses will be infeasible for the analysis of cyclic loading that would need to be modeled in medium- to high-cycle fatigue and vibratory fatigue applications. This difficulty is particularly accentuated in architected structures, for which high-resolution three-dimensional finite element analysis would be prohibitively expensive. In this work, we propose an alternative approach based on the use of novel elasto-plastic frame model with continuous flow (i.e., no sharp yield function) for modeling 3D frame and lattice structures. Rather than splitting the strains (as is done in classical plasticity) we split the deformation measures, extension, curvature and twist, into elastic and plastic components and postulate a rate type evolution rule for the plastic variables in terms of the stress resultants (axial force, bending moment, and torque). The combination of structural models together with the use of elasto-plastic operator split to solve the resulting boundary value problem allows for much faster determination of localized plasticity than continuum models can provide. The use of a continuous transition from elastic to rate independent plasticity (as opposed to an abrupt change with classical plasticity models) allows us to capture localized microplasticity and determine resulting fatigue progression using a cycle-count-free, plastic work-based approach, formulated in terms of the curvatures and resultants. We demonstrate that (a) the model is able able to reproduce the response of 3D FEA with very few elements and (b) the model has the ability to rapidly predict the fatigue life under variable amplitude combined loading with relatively few frame elements.

 $\label{lem:keywords: Low-cycle fatigue; Rate-independent plasticity; Micro-Architected materials; Geometrically-Exact beam theory; Smooth-Yielding elastic-plastic constitutive model.$

1. Introduction

Modeling the initiation and evolution of plastic deformation complex frame-like structures (such as those possible by 3D printing)—at varying length scales and for a variety of disparate applications—has been a challenge extensively examined in the literature, with a particular focus on approximating key aspects of the deformation

 $^{{\}rm *Corresponding\ author;\ Email:\ arun-r-srinivasa@tamu.edu}$

behavior without overly-onerous computational costs. The aim of this paper is to develop an approach based on a novel rate independent continuous flow model for elastoplastic frames that significantly reduces computational cost and allows for rapid evaluation of fatigue and failure response with only slight loss of accuracy compared with full FEA calculations.

For example, fractal frame structures like Menger Sponge-type micro-architectures have been considered for application in next-gen biomedical implants (see^{1,2})—their porous structure promotes superior osseointegration, and their tailorable stiffness allows better matching to that of bone, helping prevent stress-shielding and separation of the implant from the surrounding bone. However, simulation of even a single unit cell of these structures is quite challenging; recent works have required anywhere from 300 000 tetrahedral elements³ to 2 million⁴ for simulation of M=3 sponges.

In the civil engineering literature, knowledge and localization of plastic deformation within a structure has been examined extensively through limit analysis, in particular via the concept of a plastic hinge. Such plastic hinge models (or more generally "lumped plasticity models") possess the flexibility to handle both hardening and softening cases (e.g., 9, 10), and is extremely useful for gross failure analysis, this approach is severely limited for predicting fatigue where accumulation of localized microplasticity (even in the nominally elastic regime) is the determining factor before full cross sectional yielding.

There are several beam and rod models in ABAQUS that have some form of plastic deformation capabilities, however, since they assume elastic response until full cross sectional yielding they are not suitable for modeling the evolution of *microplastic* deformations in the beam; this precludes their use fatigue modeling under cyclic load that are crucial for bioimplacts. Examination of this issue is included in subsections 4.2 and 4.5.

For example, Tabatabaei et al. (2017)¹¹ employed a plastic-hinge-type formulation to create a computationally-efficient model of micro-architected structures; they allow plastic hinge formation to be determined during simulation via a von-Mises-like yield criterion stated in terms of cross-sectional stress-resultants (see equations (45) and (46) in¹¹). Similarly Challamel¹² has considered the dynamic shakedown of structures using just a one degree of freedom plasticity model.

Geometrically-exact beam theories (based on the use of direct moment curvature and twist relationships rather than 3D elasticity) have been explored in the literature for large, nonlinear deformations of elastic rods and shells for some time, ¹³ with early works exploring elastic-plastic deformations in shells due to Simo and Kennedy (1992)¹⁴ and beams due to Saje (1997, 1998, 2003). ^{15–17} Recent efforts have produced models suitable for use with elastic-plastic analysis in terms of stress resultants for large deformation of beams, ¹⁸ and elastic-visco-plastic deformations. ¹⁹ However, all the models described implement an elasto-plastic (E-P) transition that is abrupt—the material is fully elastic until a certain limit in the space of moments and forces is reached after which flow ensues. Though quite suit-

able for static failure analysis, discrete jumps from elastic to (permanent) plastic behavior (rather than smooth variation between the states) will not lend itself to capturing fatigue progression under cyclic deformation.

The situation is particularly challenging for lifetime-damage estimation under cyclic loading. This estimation has been accomplished through means of a cycle count.²⁰ If, in addition to the lengthy E-P simulation over structures with complex substructures such as a Menger sponge, a cycle count at every critical point is required, understanding the damage mechanics of multiple instances of an architected structure being designed is undoubtedly out of reach.

Time-domain analysis of complex structures using a complete elastic-plastic finite element analysis followed by a cycle count at all points through the body is often computationally intractable for cases of interest, thus workarounds are often used. Remaining in the time-domain, notch correction (see^{21–23}) and constitutive modeling (for instance using the Mroz-Garud 24 or Jiang-Sehitoglu $^{25-27}$ kinematic hardening plasticity models) of a linear-elastic FEA followed by a cycle count limited to points anticipated to present the most damage is one approach often encountered. Alternative approaches have included analyzing the progression of fatigue from the frequency-domain; ²⁸⁻³¹ by posing the problem as a statistical analysis of failure resulting from vibration, a dramatically faster calculation is possible, but at the cost of both accuracy (for some cases) and generality.

Following the work of Rajagopal and Srinivasa, 32 Wang et al. 33 formulated a smooth-yielding plasticity model for the case of a one-dimensional (1D) element stated in terms of moment and curvature, but only considered yielding resulting from bending for a single beam. In order to develop a physics based approach to fatigue, Mozafari $et \ al.^{34-36}$ extended this continuous flow plasticity model which allows fatigue damage to be accumulated through the use of total energy dissipated, without a cycle count.

The key features of the model developed here are:

- (1) A novel approach to elasto-plastic behavior of beams and frames directly in terms of stress resultants and center-line kinematics. The yield behavior is not restricted to just the nodes but throughout the structure.
- (2) A systematic procedure for the evaluation of structural parameters for different beam cross sections.
- (3) verification and validation of the results for a variety of load cases.
- (4) Application to fatigue loading predictions for combined loading conditions.

Section 2 describes the equations governing the elastic-plastic continuous flow (EPCF) which forms the core of this work, as well the important particulars of relating the generalized forces to the flow potential (subsection 2.2) and to the fatigue damage progression (subsection 2.3). Section 3 describes some salient details of the numerical approximation, in particular highlighting the variety of algorithms that can be successfully used with the EPCF model. Finally, section 4 provides

an extensive array of results to demonstrate the capabilities of the EPCF model. Beginning with a demonstration of how the required material parameters can be fit using simple results determined from cantilever beam experiments, subsections 4.2-4.4 show how the models predictions extend well to much more complicated geometries. Subsection 4.5 shows how the generalization of AMW fatigue parameter described by Mozafari $et\ al.^{34}$ to beam elements can produce results of excellent accuracy, but at significantly reduced computational cost.

2. Theory

2.1. Elastic-Plastic Continuous Flow Model (EPCF) for Beams

It is well known that when considering the yielding behavior in rods under bending and torsion (or combinations), the moment-curvature relationship does not exhibit a sharp yield point. This occurs for two reasons:

- (1) The geometry; in an E-P beam yielding begins at the outer fibers and moves towards the center so that at intermediate loads that are below the full section yielding loads, there is a mix of purely elastic and plastic regions; commercial FEM codes using classical J2 plasticity can reasonably capture this effect.
- (2) The material; under axial loading, the whole cross-section yields at the same time, nonetheless, axial stress-strain curves reveal behavior that is rarely well-captured by "perfect" elastic-plastic deformation. As can be seen in Figure 3(a), ABAQUS predicts a sharp transition in axial deformation, though this is not typically observed experimentally (see, for instance, the fits and plastic transition parameters determined in Mozafari et al. 2021³⁶).

Thus, we anticipate a clearly visible "gradual transition" from purely elastic to full plastic response in such structures; if this is not captured, plastic deformation in the structural element will be significantly under-represented. The EPCF model possesses requisite flexibility to capture both sharp transition (if needed) and gradual transition through increasing microplastic deformation.

Our aim is to model this behavior at a structural level without having to integrate across the cross section at every time step. Thus, we consider a beam in its reference configuration with its neutral axis oriented along the x-direction. Under deformation, we denote displacements of the beam along the x- (axial), y-, and z- (transverse) directions by u, v, and w, respectively. The twist angle of the beam is denoted by ϕ . For small deformations the strain and curvature measures of the beam can be written as, $\mathbf{q} = [\epsilon, \kappa_x, \kappa_y, \kappa_z]^T$, where the strains are related to the displacement as:

$$\epsilon = \frac{du}{dx}, \quad \kappa_x = \frac{d\phi}{dx}, \quad \kappa_y = \frac{d^2w}{dx^2}, \quad \kappa_z = \frac{d^2v}{dx^2}.$$
(2.1)

As in small strain plasticity, we introduce the additive splitting of the generalized strain $\mathbf{q} = \mathbf{q}_e + \mathbf{q}_p$.

The generalized load experienced by the beam is denoted by load vector $\mathbf{Q} =$ $[n, m_x, m_y, m_z]^T$, where n is the axial force, m_x is the axial moment or torque, and m_y and m_z are the bending moments around the other two axes^a The generalized load vector Q is related to the generalized strain measures using the following relationship,

$$\mathbf{Q} = \mathbb{C}(\mathbf{q} - \mathbf{q}_p) \tag{2.2}$$

The generalized modulus \mathbb{C} is a 4×4 matrix in which the diagonal elements are the section moduli under axial deformation, torsion, and bending, $(EA, GJ, EI_z, EI_y)^T$, and off-diagonal terms are zero if no phenomena such as warping are considered.

As the frame deforms the loading path traces a curve in the four-dimensional generalized strain space ${\bf q}$. Following Mozafari $et~al.^{34}$ and Jarecki $et~al.^{37}$ at every point in the generalized strain space, we will introduce a field of directions represented by 4 dimensional unit vectors N that represent the "loading direction" so that as long the generalized strain rate makes a positive angle with N, plastic flow is possible while no plastic flow occurs if the loading direction is negative, i.e.,

$$\dot{\mathbf{q}}_p \begin{cases} = 0, & \text{if } \dot{\mathbf{q}} \cdot \mathbf{N} \le 0 \\ \neq 0, & \text{otherwise} \end{cases}$$
 (2.3)

Thus, in this model, there is no sharp transition between elastic and plastic behavior. Instead, there is always plastic flow during loading.

Following Rajagopal and Srinivasa³² it can be shown that the continuity of the stress as a function of time for different load paths, and the associated flow rule of classical plasticity can be generalized by specifying that the plastic generalized curvatures evolve as:

$$\dot{\mathbf{q}}_p = \beta \mathbf{N} \tag{2.4}$$

where β is magnitude of the plastic strain rate. The value of β controls the transition from purely elastic to fully plastic flow.

To see this, we take the time derivative of (2.2) and obtain

$$\dot{\mathbf{Q}} = \mathbb{C}(\dot{\mathbf{q}} - \dot{\mathbf{q}}_p) = \mathbb{C}(\dot{\mathbf{q}} - \beta \mathbf{N}) \tag{2.5}$$

In particular, $\beta = 0$ implies no plastic flow and so (2.5) reduces to a purely elastic response.

On the other hand, if we set

$$\beta = \frac{\dot{\mathbf{q}} \cdot \mathbb{C}\mathbf{N}}{\mathbf{N} \cdot \mathbb{C}\mathbf{N}} \tag{2.6}$$

then (2.5) implies that $\dot{\mathbf{Q}} \cdot \mathbf{N} = 0$ and fully plastic flow ensues in the direction \mathbf{N} . In other words, we obtain a plastic hinge.

^aSince this is based on Euler-Bernoulli beam theory, the shear forces do no work and so are not included in the list.

6 D. Jarecki et al. 2023

The central idea here is to choose a constitutive relation for β that (a) satisfies (2.3), (b) ensures rate independent behavior, and (c) ensures that the the response smoothly transitions from elastic to fully plastic flow when the fully plastic yielding of the cross section is reached.

In order to achieve this, we define a "gross" or "fully plastic" flow function $F(\mathbf{Q}) \leq 0$ such that $F(\mathbf{Q}) = 0$ represents section yielding. We then specify the flow direction \mathbf{N} to be:

$$\mathbf{N} = \frac{\frac{\partial F}{\partial \mathbf{Q}}}{\left| \left| \frac{\partial F}{\partial \mathbf{Q}} \right| \right|} \tag{2.7}$$

Finally, we specify the constitutive relation for the plastic strain rate magnitude β to be:

$$\dot{\mathbf{q}}_p = \left[1 + \tanh\left(\alpha(\mathbf{N})F(\mathbf{Q})\right)\right] \left\langle \frac{\mathbb{C}\mathbf{N} \cdot \dot{\mathbf{q}}}{\mathbf{N} \cdot \mathbb{C}\mathbf{N}} \right\rangle \mathbf{N}$$
 (2.8)

Where, as previously, $\langle \bullet \rangle$ denotes Macaulay brackets. Note that the tanh function ensures a smooth transition from 0 to 1. The transition function $\alpha(\mathbf{N})$ controls the transition from microplastic to bulk flow in the frame. Its dependence on the flow direction \mathbf{N} is vital to account for the ability to model the response due to combined loading as we shall see later. Small values of α represent a very gradual transition from microplastic to section yield such as that encountered in bending or torsion while large values of α represents a more abrupt transition.

This completes the description of the smooth-yielding model developed for beams; the only remaining challenge is to determine a suitable means of determining how applied moments and forces push the model towards elastic-plastic behavior. The form of the yield function (or flow potential, in the context of this work) in terms of stress resultants is a nontrivial matter, examined at some length in the literature (see, in particular, sections 1.4 and 1.5 from;³⁸ for a more recent examination, see¹⁸). The specific form employed in this paper is discussed in the following subsection 2.2.

2.2. Relating the flow potential to the section yielding conditions

To exploit the material constants used with the 3D stress-strain formulation of the model, we need a means of relating the generalized forces \mathbf{Q} to the yield stress of the material and the cross section of the beam. For our purposes, the plastic limit moduli, well-reported in the structural literature (see, for instance, ³⁹ for torsion and ⁴⁰ for bending), are suitable.

The flow function is given by a von Mises-like yield condition:

$$F(\mathbf{Q}) = f(\mathbf{Q}) - \sigma_y = \left[(\mu_n n)^2 + (\mu_x m_x)^2 + (\mu_y m_y)^2 + (\mu_z m_z)^2 \right]^{1/2} - \sigma_y \quad (2.9)$$

In Equation 2.9, σ_y denotes the yield stress and the μ parameters provide a bridge between stress and the generalized loading.

As mentioned previously, significant effort has been expended to determine a form for the yield function/flow potential that is suitable for use with stress resultants. Causing particular issue is the fact that the generalized-load yield surface—in addition to being geometry-dependent—is likely not a hypersphere, or even a hyperellipse.

Herrnbock *et al.*, ¹⁸ for instance, suggest fits to the following form for a flow potential in terms of stress resultants:

$$\left| \frac{n_1}{n_{1y}} \right|^{\alpha} + \left| \frac{n_2}{n_{2y}} \right|^{\alpha} + \left| \frac{n_3}{n_{3y}} \right|^{\gamma} + \left| \frac{m_1}{m_{1y}} \right|^{\delta} + \left| \frac{m_2}{m_{2y}} \right|^{\delta} + \left| \frac{m_3}{m_{3y}} \right|^{\xi} - 1 = 0$$
 (2.10)

where the n_i are forces, m_i are moments, and α , γ , δ , ξ are potentially distinct exponents. Mollica et al.⁴¹ have shown a systematic procedure for obtaining flow potentials of any degree of complexity. Such an approach can be tailored to a wide range of response possibilities but at the cost of increasing the amount of curve fitting. Though use of specific carefully-tailored flow potentials would undoubtedly improve accuracy. However, in order to illustrate the efficacy of our approach, we demonstrate in this paper that the EPCF model can determine suitable fatigue predictions, even when only using the simplest models with very minimal curve fitting using a hyper-ellipsoid flow potential.

With a specific form chosen posited for the flow potential, we can now determine the surface normal (equation (2.7)) as:

$$\mathbf{N} = \frac{1}{\sqrt{(\mu_n n)^2 + (\mu_x m_x)^2 + (\mu_y m_y)^2 + (\mu_z m_z)^2}} \begin{cases} \mu_n^2 n \\ \mu_x^2 m_x \\ \mu_y^2 m_y \\ \mu_z^2 m_z \end{cases}$$
(2.11)

We report the forms of the limit moduli for two cross-sections, though of course, numerous others are available in the literature, or can be derived using techniques of the theory of elasticity. (Note that for all cases, we take $\mu_n = 1/A$.) For a beam of rectangular cross-section oriented along the x-axis, defined by height h oriented along the y-axis and width w oriented along the z-axis, we have:

$$\mu_x = \frac{2\sqrt{3}}{a^3 \left(\frac{b}{a} - \frac{1}{3}\right)}; \quad \mu_y = \frac{4}{hw^2}; \quad \mu_z = \frac{4}{h^2 w}$$
(2.12)

Where μ_x corresponds to torsion and μ_y, μ_z to bending, and a = max(h, w) and b = min(h, w). For the particular case of a square cross-section, the simpler expressions $\mu_x = 3\sqrt{3}/h^3, \mu_y = \mu_z = 4/h^3$ are obtained.

For a beam oriented along the x-axis possessing an elliptical cross-section, described by major and minor axis (a + b) and (a - b), respectively, we have the following:

$$\mu_x = \frac{3\sqrt{3}}{2\pi a^3 \left(1 - 4.5\left(\frac{b}{a}\right)^2 + 4\left(\frac{b}{a}\right)^3\right)}; \quad \mu_y = \frac{3}{4(a+b)(a-b)^2}; \quad \mu_z = \frac{3}{4(a+b)^2(a-b)}$$
(2.13)

8 D. Jarecki et al. 2023

Assuming that the major axis is oriented along the y-axis and the minor axis along the z-axis. Obviously, the bending parameters are flipped if the opposite arrangement is true. For the particular case of a circular cross section (radius R) the simpler expressions $\mu_x = 3\sqrt{3}/(2\pi R^3)$, $\mu_y = \mu_z = 3/(4R^3)$ are obtained.

Note that for non-circular cross-sections, if significant torsional deformation is anticipated, then the generalized modulus $\mathbb C$ should be modified to include warping; these constants alone will not compensate for this effect with an unmodified modulus.

2.3. Damage accumulation based on accumulated microplastic work(AMW) for Fatigue Failure Criterion in Smooth-Yielding Model

Mozafari et al. (2021),³⁶ determine progress to fatigue in terms of accumulated microplastic work (AMW), using the following expression:

$$\eta_{stress}(t) = \int_0^t \boldsymbol{\sigma} : \dot{\boldsymbol{\varepsilon}}^P dt \tag{2.14}$$

where : denotes the tensor contraction. When AMW (in units of energy per volume) reaches critical value η_f , fatigue failure is predicted to occur. We suggest an analogous expression in terms of force resultants:

$$\eta_{FR}(t) = \int_0^t \mathbf{Q} \cdot \dot{\mathbf{q}}^P dt \tag{2.15}$$

Here we have AMW in terms of individual beam elements, in units of energy per *length*.

Below, we compare the AMW calculations for simple loads (axial, bending, and torsion) of a cantilever beam of length L oriented with its neutral axis along the x-axis and constant, symmetric cross-section of area A, which should allow us to accurately approximation η_{stress} from η_{FR} .

Axial Deformation. For the small strain approximation $(\varepsilon_{xx} \approx du/dx)$, both AMW parameters are related by cross-sectional area (as should be expected given the units):

$$\eta_{FR}(t) = \int EA\left(\frac{du}{dx} - \varepsilon^P\right)\dot{\varepsilon}^P dt = A\left(\eta_{stress}(t)\right)$$

Bending Deformation. We limit ourselves to a beam with a square (height, h) or circular (radius, r) cross-section; For the loading described, the maximum stress will occur at $z = \pm h/2$ and $z = \pm r$ for the square and circular cross-sections, respectively.

For the case in which the cantilever beam so described is loaded with a transverse load on the neutral axis, the maximum uniaxial stress is given by:

$$\sigma_{xx} = \frac{Mz}{I} = -zE\left(\frac{d^2w}{dx^2} - \kappa_z^p\right)$$

Recognizing that for the beam loaded in this way subject to the small strain approximation, we have $\varepsilon_{xx}^P \approx z \kappa_z^P$, we can relate the AMW in terms of stress with that determined using the generalized force and curvature relationships upon substitution for the particular form of the moment of inertia.

$$\eta_{FR}(t) = \int EI\left(\frac{d^2w}{dx^2} - \kappa_z^p\right) \dot{\kappa}_z^P dt \tag{2.16}$$

In the case of a square cross-section (where $I = (h^4/12) = (A/3)(z^2)$):

$$\eta_{FR}(t) = \frac{A}{3} \left(\int zE \left(\kappa_z - \kappa_z^P \right) (z\dot{\kappa}_z^P) dt \right) = \left(\frac{A}{3} \right) \eta_{stress}(t)$$

In the case of a circular cross-section (for which $I=(\pi r^4/4)=(A/4)(z^2)$):

$$\eta_{FR}(t) = \frac{A}{4} \left(\int zE \left(\kappa_z - \kappa_z^P \right) (z\dot{\kappa}_z^P) dt \right) = \left(\frac{A}{4} \right) \eta_{stress}(t)$$

Torsional Deformation. We follow the same process for a cantilever loaded by a twisting moment, T around the x-axis which produces angular rotation ϕ . The maximum uniaxial stress in this same cantilever is given by:

$$\sigma_{xy} = \frac{Mr}{J} = rG\left(\frac{d^2\phi}{dx^2} - \kappa_x^p\right)$$

Recognizing that for the beam loaded in this way subject to the small strain approximation, we have $\varepsilon_{xy}^P \approx r \kappa_x^P$, we can relate the AMW in terms of stress with that determined using the generalized force and curvature relationships upon substitution for the particular form of the polar moment of inertia.

$$\eta_{FR}(t) = J \int G\left(\kappa_x - \kappa_x^p\right) \dot{\kappa}_x^P dt$$

In the case of a square cross-section (where $I = (h^4/6) = (2A/3)(z^2)$):

$$\eta_{FR}(t) = \frac{2A}{3} \left(\int zG\left(\kappa_x - \kappa_x^p\right) \left(z\dot{\kappa}_x^P\right) dt \right) = \left(\frac{2A}{3}\right) \eta_{stress}(t)$$

In the case of a circular cross-section (for which $J = (\pi r^4/2) = (A/2)(z^2)$):

$$\eta_{FR}(t) = \frac{A}{2} \left(\int zG\left(\kappa_x - \kappa_x^p\right) (z\dot{\kappa}_x^P) dt \right) = \left(\frac{A}{2}\right) \eta_{stress}(t)$$

Note that we must multiply these proportionality factors by (1/2) in this case, however, due to the fact that shear multiplication terms $\sigma_{ij}\varepsilon_{ij}^p$, $i \neq j$ appear twice in a tensor contraction

The foregoing discussion suggests the following form for η , used throughout this work:

$$\eta(t) = \frac{1}{A} \int \left(n\dot{\varepsilon}^P + \phi_{bend}(m_y \dot{\kappa}_y^P + m_z \dot{\kappa}_z^P) + \phi_{tors}(T\dot{\kappa}_x^P) \right) dt$$
 (2.17)

Where for a square cross-section $\phi_{bend} = \phi_{tors} = 3$, and for a circular cross-section $\phi_{bend} = \phi_{tors} = 4$. This form is suitable for simple loadings, but undoubtedly

becomes inaccurate for more complex ones; nonetheless, as demonstrated in the next section, we can still use this to leverage the model from Mozafari $et\ al.^{34-36}$ for excellent fatigue life predictions, but at significantly lower computational cost.

3. Numerical Approximation

3.1. Elastic-Plastic Boundary Value Problem

Assuming no body force, the generalized force balance equations for an Euler-Bernoulli beam oriented along the x-axis (or rotated to lie along this direction) can be written as:

$$\int_{x_{-}}^{x_{b}} \left[n \frac{du}{dx} + m_{x} \frac{d\phi}{dx} + m_{y} \frac{d^{2}w}{dx^{2}} + m_{z} \frac{d^{2}v}{dx^{2}} \right] dx = 0$$
 (3.1)

Selecting Lagrange test function ψ for axial displacement and small rotation due to torsion, and Hermite cubic φ for the transverse displacements and their first derivative, we substitute the individual equations contained in (2.2) into equation (3.1); partitioning (3.1) with respect to distinct virtual displacements (denoted below with a δ before the appropriate test function), we have:

$$\int_{x_a}^{x_b} \left[EA \left(\frac{d\psi}{dx} - \epsilon_p \right) \right] \frac{d\delta\psi}{dx} dx = 0, \quad \int_{x_a}^{x_b} \left[GJ \left(\frac{d\psi}{dx} - (\kappa_x)_p \right) \right] \frac{d\delta\psi}{dx} dx = 0, \quad (3.2)$$

for axial and torsional deformation on a given element from x_a to x_b and

$$\int_{x_a}^{x_b} \left[EI_z \left(\frac{d^2 \varphi}{dx^2} - (\kappa_z)_p \right) \right] \frac{d^2 \delta \varphi}{dx^2} dx = 0, \quad \int_{x_a}^{x_b} \left[EI_y \left(\frac{d^2 \varphi}{dx^2} - (\kappa_y)_p \right) \right] \frac{d^2 \delta \varphi}{dx^2} dx = 0$$
(3.3)

for bending about both transverse axes.

Numerically, we can accurately and expediently solve the flow rule and transverse force balance over the finite element mesh using operator split: that is, any given load increment is split into two steps, (i) an elastic step—freezing the plastic curvature—and (ii) a plastic step—freezing the plastic rate.

To describe the formulation over a single reference element oriented along the x-axis from x_a to x_b , we introduce discrete nodal variables u_j , ϕ_n , v_J , and w_N representing the axial displacement, twist, and the transverse displacements and bending rotations along the y- and z-directions, respectively. The axial displacement u_j and twist ϕ_n are interpolated using Lagrange interpolation functions, denoted below by ψ . To maintain continuity for both the transverse displacement and the bending rotation (related to the transverse displacement by the first derivative for an Euler-Bernoulli beam), we employ Hermite cubic interpolation functions nodal variables v_J and w_N . The form for Lagrange and Hermite interpolation functions as well as the particulars of Gauss-Point numerical integration are well-known see e.g. 42

For the deformations described by this model, we have:

$$\left(\int_{x_{a}}^{x_{b}} \left[EA \frac{d\psi_{i}}{dx} \right] \frac{d\psi_{j}}{dx} dx \right) u_{j} = \int_{x_{a}}^{x_{b}} \left[EA \epsilon_{p} \right] \frac{d\psi_{i}}{dx} dx
\left(\int_{x_{a}}^{x_{b}} \left[GJ \frac{d\psi_{m}}{dx} \right] \frac{d\psi_{n}}{dx} dx \right) \phi_{n} = \int_{x_{a}}^{x_{b}} \left[GJ(\kappa_{x})_{p} \right] \frac{d\psi_{m}}{dx} dx
\left(\int_{x_{a}}^{x_{b}} \left[EI_{z} \frac{d^{2}\varphi_{I}}{dx^{2}} \right] \frac{d^{2}\varphi_{J}}{dx^{2}} dx \right) v_{J} = \int_{x_{a}}^{x_{b}} \left[EI_{z}(\kappa_{z})_{p} \right] \frac{d^{2}\varphi_{I}}{dx^{2}} dx
\left(\int_{x_{a}}^{x_{b}} \left[EI_{y} \frac{d^{2}\varphi_{M}}{dx^{2}} \right] \frac{d^{2}\varphi_{N}}{dx^{2}} dx \right) w_{N} = \int_{x_{a}}^{x_{b}} \left[EI_{y}(\kappa_{y})_{p} \right] \frac{d^{2}\varphi_{M}}{dx^{2}} dx \tag{3.4}$$

where the lower-case indices shown above take the values of 1 and 2 indices per element, and the upper-case indices (associated with the Hermite cubic test functions) take the values 1 through 4 indices per element. We can state this concisely (treating the right hand side as a plastic forcing contribution) as $[K_{ij}](\Delta_i) = (F_p)_i$, where, now in this case, j varies through the 12 DOFs associated with a single finite element.

In equation (3.4), we take plastic curvatures as values from the previous load increment, \mathbf{q}_n^n ; this constitutes the first update step of the algorithm, in which the current values of the curvature, that is \mathbf{q}^{n+1} , are obtained. The algorithm selected below is justified noting that for almost all inelastic processes, the loading vector and flow direction do not change much within a load increment.⁴³

3.2. Update of Plastic Variables

We state an algorithm described in³⁷ in a form suitable for use with the momentcurvature model here as Algorithm 1. The plastic update step takes the configurational variables at the (n+1)th step and the plastic variables at the nth step to produce the increment in plastic variables $\Delta \mathbf{q}_p$. The change in the plastic variables within each load step needs to be updated consistent with the yield condition and flow rule. We denote the nth load step flow direction by \mathbf{N}^n . Considering equation (2.4) we arrive at the following condition on plastic strain rate β :

$$\beta = \left[1 + \tanh\left(\alpha(\mathbf{N}^n)F(\mathbf{q}^{n+1}, \mathbf{q}_p^{n+1})\right)\right] \left\langle \frac{\mathbb{C}\mathbf{N}^n \cdot (\mathbf{q}^{n+1} - \mathbf{q}^n)}{\mathbf{N}^n \cdot \mathbb{C}\mathbf{N}^n} \right\rangle$$
(3.5)

```
Result: Computes \mathbf{q}^{n+1}, Given \mathbf{q}^n
  2 START: \Delta \mathbf{q}_p = 0, ERROR = 1, TOL = 10^{-6}, i = 0, imax;
  \mathbf{g} \mathbf{q} \longleftarrow \mathbf{q}^{n+1};
  \mathbf{5} while ERROR > TOL and \mathbf{i} < \mathbf{imax} \ \mathbf{do}
                \mathbf{q}_p \longleftarrow \mathbf{q}_p^n + \Delta \mathbf{q}_p;
                \Delta \mathbf{q} \longleftarrow \mathbf{q} - \mathbf{q}^n;
               \phi = ||\Delta \mathbf{q}_p||;
  8
  9
                Compute the loading direction \mathbf{N} = \mathbf{N}(\mathbf{q}, \mathbf{q}_p);
 10
               if L := \mathbb{C}\mathbf{N} \cdot \Delta \mathbf{q}/\mathbb{C}\mathbf{N} \cdot \mathbf{N} > 0 then
11
                        \beta = \beta(\mathbf{q}, \mathbf{q}_p);
 12
                       \theta = -\frac{\partial \beta}{\partial \mathbf{q}_p} \cdot \mathbf{N};
d\mathbf{q}_p = \frac{(\beta + \theta\phi)L}{1 + \theta L} \mathbf{N};
 13
 14
 15
                 d\mathbf{q}_{p}=0;
 16
17
 18
                ERROR \longleftarrow ||d\mathbf{q}_p - \Delta\mathbf{q}_p||;
                \Delta \mathbf{q}_p \longleftarrow d\mathbf{q}_p;
19
20
               i \longleftarrow i+1
21
22 end
23
\mathbf{24} \ (\mathbf{q}^{n+1}, \mathbf{q}_p^{n+1}) \longleftarrow (\mathbf{q}, \mathbf{q}_p);
```

Algorithm 1: Picard Iteration performed at each Gauss point of EP BVP; \mathbf{Q}_i^n denotes the temporary generalized forcing values available after iteration i

3.3. Determination of Model Structural Parameters

Since this is a frame model, the response is governed not only by type of loading, but also by the cross-sectional geometry. For a given geometry, the following features of the elastic-plastic deformation were considered essential to the proper modeling of the fracture behavior.

- (1) Initial slope of force-displacement curves (Section moduli, EA, EI, GJ);
- (2) Perfect plasticity limit forces/moments for single-load cases (Yield stress, σ_y);
- (3) Elastic-plastic behavior in transition region (Transition parameter, α).

The determination of the first two categories is straightforward, following directly from the geometry and standard experimental procedures; alpha can be

modified for each single-loading case separately until a suitable match is obtained. Figure 1 shows this process for the case of pure axial loading.

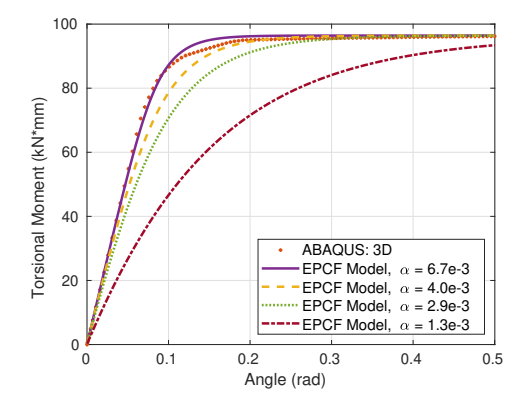


Fig. 1: Even if the underlying material has a sharp transition from elastic to plastic, the structural response under bending and torsion will have a smooth transition to plastic response. The elastoplastic continuous flow (EPCF) model can be tuned to better approximate the E-P transition region via judicious selection of α . This is crucial for fatigue calculations based on damage accumulation

Given force-displacement and moment-curvature experimental data (or data from a high-fidelity simulation), we suggest the following methods to assess the accuracy of the E-P beam model and to obtain replicable fits to the given material parameters.

Method 1: Residuals. The two residuals below can be employed to assess accuracy of the continuous-yielding E-P beam model:

$$R_{1} = \sum_{i=1}^{4} ||\max(Q_{i}) - \max(Q_{i}^{exp})||$$

$$R_{2} = \sum_{i=1}^{4} \sum_{q_{i}(t_{j})=q_{i}(t_{0})}^{q_{i}(t_{f})} ||\kappa_{qQ}(t_{j}, q_{i}, Q_{i}) - \kappa_{qQ}^{exp}(t_{j}, q_{i}, Q_{i})||$$
(3.6)

where values with the superscript "exp" denote quantities obtained experimentally or numerically from a (presumed) higher fidelity model (such as a full 3D continuum-based simulation). For the first residual perfect plasticity is assumed (so that a plateau value is actually attained); the greater the value of R_1 , the greater the difference between the numerically predicted plateau value for a given element of the generalized load vector Q_i and the experimental value Q_i^{exp} . For the second residual, a forward difference approximation of the numerical (EPCF) curvature, $\kappa_{qQ}(t_j, q_i, Q_i)$ is compared with the experimentally determined values, $\kappa_{qQ}^{exp}(t_j,q_i,Q_i)$, in the EP transition region, indexed along generalized displacement values from (user-selected) t_i to t_f ; the curvature measure is given as:

$$\kappa_{qQ}(t_j, q_i, Q_i) = \frac{(q_i(t_{j+1}) - q_i(t_j)) |Q_i(t_{j+1}) - Q_i(t_j)|}{(Q_i(t_{j+2}) - 2Q_i(t_{j+1}) - Q_i(t_{j+1}))^{3/2}}$$
(3.7)

No residual is included for the initial (elastic) slope—it is determined from standard experiments, and no modification is required for use here—, or for the yield stress—once a plateau value is identified for one of the force resultant of interest, the yield stress follows from the plastic limit moduli.

Method 2: Slope Intersection.

For the case of the elastoplastic beam and frame response, we identify 4 characteristic features of the response (see figure 2 as well as the discussion in⁴⁴ and,⁴⁵ in which this approach is applied to nonlinear models of biological fibers). (1) the initial slope which represents the elastic stiffness D_0 , (2) the final slope D_{∞} which represents the flow behavior after full section yielding and is related to the flow function g hardening characteristics (3) the intersection point (Q_0, q_0) between the initial and final slope lines (related to the form of the flow function) and (4) the point (Q_1, q_0) corresponding to the drop in the stress due to continuous flow (related to the transition parameter α). We note that this method reduces to standard definitions of yield if the structure has a sharp yield point; it also separates the "transient region" from the full section yield thus obviating the need for complex hardening rules to account for this phenomenon. This approach provides an easily-replicable method for fitting data in an EP simulation.

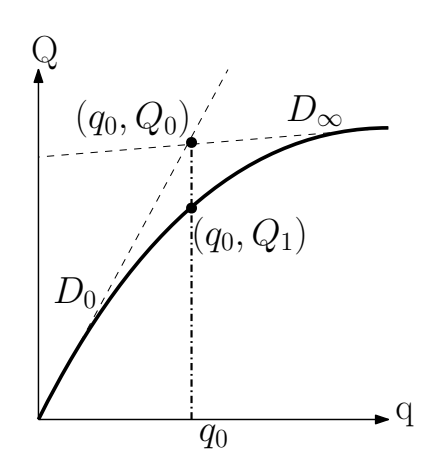


Fig. 2: Slope intersection method for fitting our elastic-plastic deformation model to data. The key measurements that will be used for the parameter fitting are (1) the initial slope D_0 , (2) the final slope D_{∞} (3) the point of intersections (Q_0, q_0) and the point (Q_1, q_0) that represents deviation from the sharp yield.

In the case of the EPCF model, the smoothness parameter α selected should be the one that minimizes error at the point on the stress-strain (or generalized

Table 1: List of the transition function α values determined for pure loading cases; all values are shown in units of 1/MPa. These are used in equation (3.8)

Cross-Section	α_{ax}	α_{bend}	α_{tors}
Square	0.1	0.00571	0.00667
Circle	0.1	0.00571	0.00667

force-displacement) curve directly beneath the intersection point of the bilinear representation generated from the two slopes. Figure 2 shows what this fitting method looks like graphically.

Figure 3 below shows single load simulations, representative of the type of data that can be used to fit the material parameters needed for the elastic-plastic continuous flow beam elements. For each of the different load types, different α values are determined; the values obtained for the square and circular cross-sections under the loading conditions considered above are listed in Table 1.

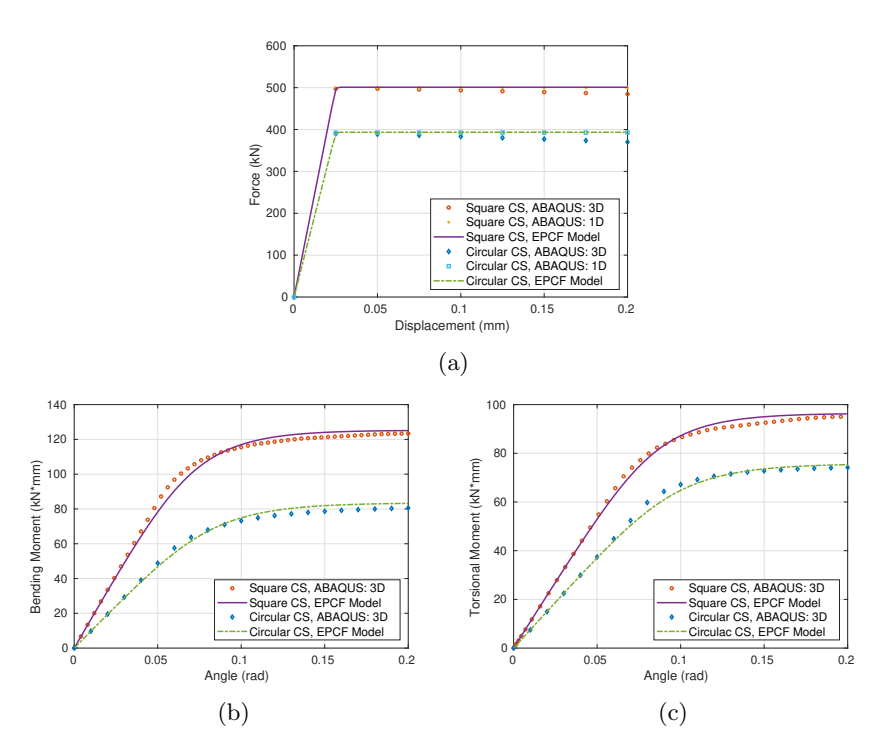


Fig. 3: Single load (a) axial, (b) bending, and (c) torsion simulation used to fit α parameter in EPCF model for rectangular and circular cross-sections.

We will set the transition function $\alpha(\mathbf{N})$ to be simply linear in the direction of

16 D. Jarecki et al. 2023

loading, i.e.,

$$\alpha(\mathbf{N}) = \sum_{i=1}^{3} \alpha_i N_i \tag{3.8}$$

With the α_i being obtained from curve fitting the "pure" loading cases: α_1 being fit to axial loading (see Fig. 3(a)) α_2 being fit to pure bending (see Fig. 3(b)) and α_3 being fit to pure torsion (see Fig. 3(c)). The values of α_i for square and circular cross sections can be seen in Table 1.

4. Results

4.1. Monotonic Combined Loading Studies

The predictions of the EPCF model was compared to finite element (FE) simulations performed in ABAQUS. The design of the structures used is shown in Figure 4.

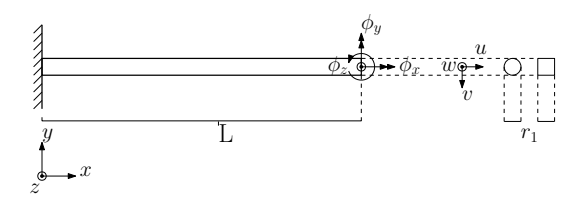
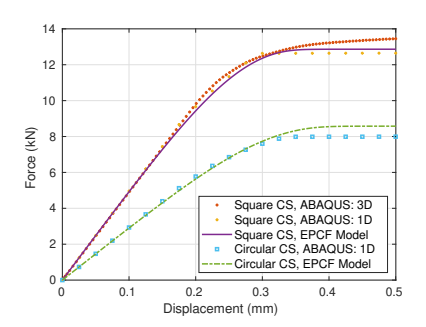


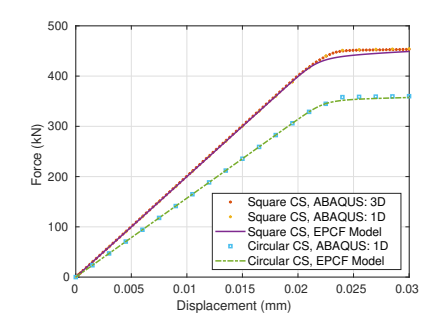
Fig. 4: Cantilever simulated in ABAQUS with C3D8 and B33 elements for comparison against predictions of continuously-yielding EP beams. Different combinations of displacements and rotations were applied to the beam and the tip deflection versus the applied load was compared (see also Fig. 5

One end of the beam was fully constrained, and loads were applied on the other end of the beam. Every node/element at the end surface was coupled to a single reference point and individual and combined loads such as vertical displacement, and rotations were imposed on that point.

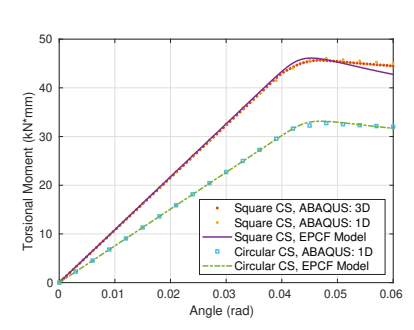
Figure 5(a) shows the results obtained for loading via an off-axis displacement (i.e., flexure, not pure bending); the EPCF model captures the behavior predicted in ABAQUS fairly well here.

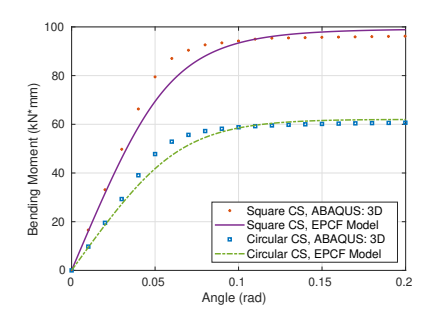
Figure 5b,c,d,e shows the comparison between the smooth-yielding model for the tension-torsion combined loading and bending-torsion case, respectively, for both square and circular cross-sections. Notice the prominent mismatch in generalized load plateau height for the case of torsion in the square cross-section; this is undoubtedly due to the omission of warping in the EPCF formulation. Future modifications to include warping will likely capture the final generalized load plateau for non-circular cross-sections under torsion much more accurately.





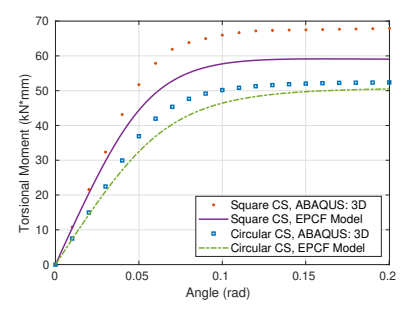
(a) Force desiplacement response due to (b) Force displacement response due to transvers loading load simultaneous Axial load and Twist





(c) Torque vs. twist response due to simultaneous Axial load and Twist:

(d) Moment vs transverse rotation response due to combined bending and torsion



(e) Torque vs Twist angle response due to combined bending and torsion

Fig. 5: Results of simultaneous monotonous end loading of a cantilever beam: comparison between ABAQUS 3D and the EPCF model.

4.2. Monotonic and Cyclic Loading of Beams under Various End Loadings

Once the smoothness parameter has been appropriately selected using single-load input as described previously, the calibrated results extend well to handle cyclic deformations. A comparison between cyclic deformations predicted by ABAQUS against those from the EPCF model is shown below in Figure 6.

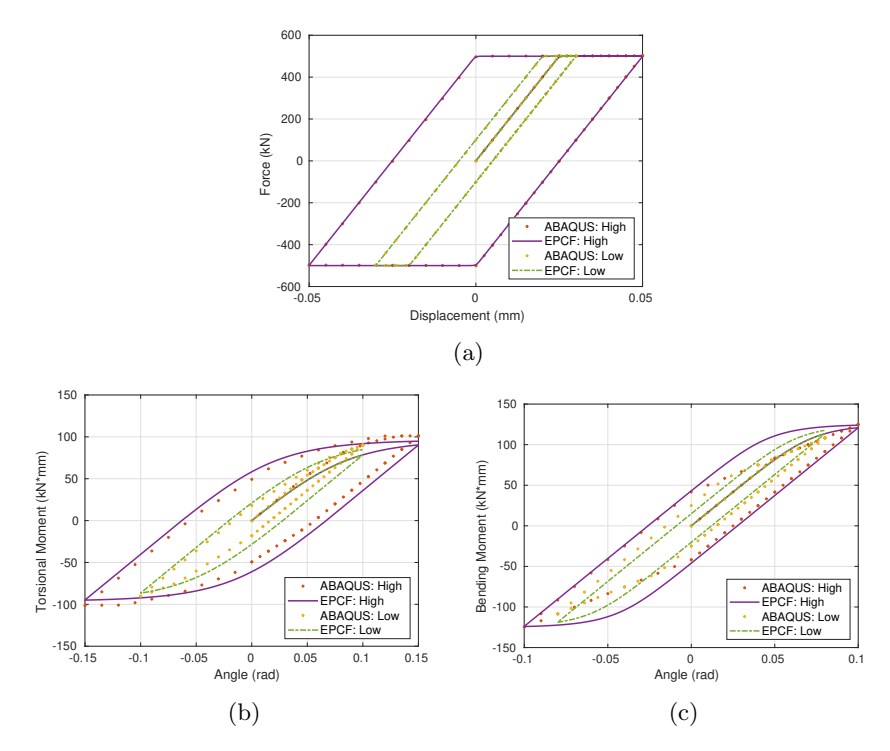


Fig. 6: Cyclic deformation comparison between ABAQUS and the EPCF model for single load (a) Tension, (b) Torsion, and (c) Bending. The continuous-yield behavior of the EPCF model allows it to compute fatigue damage from the accumulated microplastic work, which would not be possible with current commercial code.

As noted before, the sharp transition of J2 plasticity (and the piecewise jump in behavior in the hardening model used in ABAQUS) will not capture the continuous accrual of plasticity (and associated damage from microplastic work), so—though simulations using models in this class are useful as a comparison—they would not be suitable for the AMW fatigue calculation described here.

4.3. Deformation of Frames

In this section we show the efficacy of the new beam model in the simulation of the response of more complex structures. We begin with the consideration of two-dimensional (2D) and three-dimensional (3D) portal frames. We compare the model response with that of an ABAQUS 3D model with a square shaped cross section for every vertical support (centerline length $L_2=11.5$ mm) and horizontal beam

(centerline length $L_1 = 9$ mm). The width w and height h of the cross sections were 1 mm. The end surfaces (3D ABAQUS) and end nodes (EPCF) of the vertical support in the frame were constrained. The nodes/elements at the shared sections between a support and a beam at a top corner of a frame were coupled to a reference node and loads were applied to that assigned node accordingly.

Figure 7 (c) shows the region where the displacement was applied to deform the three-dimensional frame. The size of the applied loading region was selected to be big enough to eliminate any erroneous localized deformation while still being small enough to simulate a point-wise loading condition on a frame.

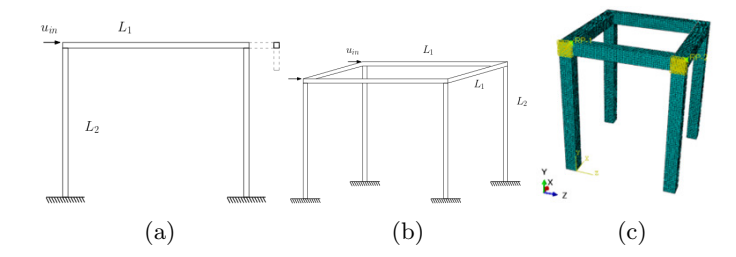


Fig. 7: Structures simulated in ABAQUS with C3D8 elements for comparison against predictions of continuous-flow EP beam elements. (a) 2D Portal Frame, (b) 3D Portal Frame; (c) Finite element mesh used for 3D portal frame in ABAQUS, with regions of load application highlighted.

The three-dimensional eight node brick element C3D8 element was used to simulate both beams and frames. Notably, the geometry and applied load in the 2D frame were in 2D but a 3D element was used to simulate it when the square shaped cross section of the frame was considered.

Three loading cases were considered; for both the 2D and 3D portal frames, applied displacement of $u_{in} = 5$ mm were used (Figure 7), giving one case for the 2D frame, one for the 3D frame in which both applied displacements were in the same direction, and one final case for the 3D frame in which the applied displacements were in the opposite direction (push-pull).

The force-displacement curves are presented and compared well to the analytical results as shown in Figures 8 - 9, with only the push-pull case exhibiting discrepancies with the result predicted by ABAQUS.

The push-pull 3D frame plateau loads predicted by the EPCF model and ABAQUS differed somewhat (Figure 9(b)); it is likely that this is due to torsion. For the push-pull case, the vertical support beams twist around the central axis somewhat, and, because the cross-section employed is non-circular, warping is anticipated. Modifications to the EPCF model to include warping would likely address this. Nonetheless, we are able to effectively produce results with significantly reduced computational effort that reasonably represent the anticipated deformation

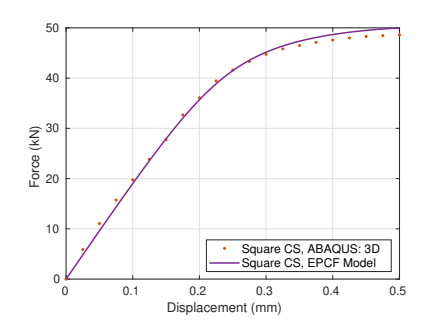


Fig. 8: Load displacement at point of application on 2D portal frame.

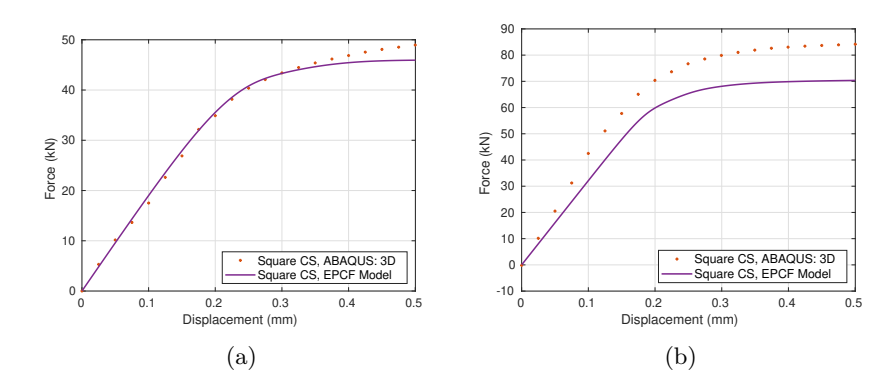


Fig. 9: Load displacement at point of application of 3D portal frame; (a) applied displacements in same direction, (b) applied displacements in alternate directions. The descrepancy in figure 23 is due to warping which is not accounted for in the current formulation

results of complex loadings and structures, using only data gleaned from material parameters, geometry, and simple fits to pure load cases, which was our intended result.

4.4. Deformation of Microarchitected Geometries

In this subsection, we demonstrate how the EPCF model (with judicious choice of section moduli parameters) can be used to model the elastic-plastic deformation in complex microarchitected geometries.

We consider the recent work of Kushwaha $et\ al.^4$ The fractal Menger sponge geometry (created by repeating, progressively smaller, self-similar removals of a cube from an original solid cube) has been evaluated as a potential design for prostheses, for two reasons principally: first, the tailorable architecture allows a better match between the elastic modulus of bone and the prosthesis, and second, the porous

structure promotes superior osseointegration as the surrounding bone heals and accepts the prosthesis. As an engineering problem, however, the Menger sponge presents a challenge; clearly predictive analysis must be performed before prostheses with these novel designs can be cleared for use in humans, but meshing itself is a challenge. Prediction of the likely fatigue life is computationally prohibitive.

Kuswaha et al.⁴ performed numerical simulation of various Menger sponge structures using ANSYS Mechanical APDL; their mesh convergence analysis revealed that they required about 2 million quadratic tetrahedral elements (SOLID 187). We aim to replicate the qualitative behavior they observed, but with dramatically fewer elements.

We referred to Kuswaha's provided materials, using an elastic modulus of 1.55 GPa and a Poisson ratio of 0.3. Taking the specific yield stress of 40.70 for the solid specimen (denoted L0; see Kuswaha, Table 3) and the reported density (1.25 g cm⁻3), we have a yield stress of 50.875 kPa.

From Kushwaha's description of the Menger sponge compressive tests, and their reported boundary conditions for the base of the sponge in their ANSYS simulations, we fix displacements and rotations in for all nodes on the base of our selected meshes. Determining the particulars of the compressive loading, however, is not as clear. The experimental loading used a central pillar to press the specimen, partially distributing this load via a top plate (see Figure 5 in⁴), but the relative size of the pillar is not reported. Assuming that the top plate would not distribute the load uniformly but that greatest contact would be experienced at the center of the specimen (and in the absence of any details on their chosen numerical implementation) we employed a loading profile windowed with the square root of a sine function centered over the largest (centermost) cavity.

The Menger sponge is symmetric; arbitrarily, we orient the bottom part of the sponge in the xy-plane (and the bottom part of the 2D reduction in the x-plane) at z=0. Denoting side length by L (equal to 5 cm, to match the stated geometry in Kushwaha et al., we have selected the following form for the boundary condition at the top face (z = L) of the 2D reduction (Sierpinski carpet):

$$w_{app}(x) = \sqrt{\sin\left(\frac{\pi x}{L}\right)} \tag{4.1}$$

where w_{app} denotes the maximum applied displacement boundary condition in the z-direction (gradually approached as a ramp loading from zero to maximum over the top surface). Similarly, for the 3D simulation, we employ the loading boundary condition:

$$w_{app}(x,y) = \sqrt{\sin\left(\frac{\pi x}{L}\right)\sin\left(\frac{\pi y}{L}\right)}$$
 (4.2)

For both the 2D and 3D simulations, we reduced the computational load by trying to enforce symmetry down the center-line (2D) or center-planes (3D). For the 2D case, we maintained $u = \theta_y = \theta_z = 0$ at the centerline (x = L/2); for the 3D case, we enforced $u = v = \theta_y = \theta_z = 0$ at the center-planes (x = L/2 and y = L/2).

22 D. Jarecki et al. 2023

Table 2: List of section moduli and flow potential parameters used for all levels of Sierpinski carpet simulation (consistent discretization allows the same values to be used for each). Note that, in this case, symmetry causes $EI_x = EI_y$ and $\mu_y = \mu_z$, so only one value is reported for bending.

EA (kN)	EI (kN/mm)	GJ (kN/mm)	$\mu_n(\text{mm}^{-2})$	$\mu_y(\mathrm{mm}^{-3})$	$\mu_x(\mathrm{mm}^{-3})$
1.33e3	9.49e1	7.27e1	1.17	5.04	6.55

To attempt replication of the behavior of solid regions of the Menger sponge with 1D beam elements, section moduli corresponding to elements large enough along the cross-section that they would touch surrounding elements are used; the parameters relating the flow potential to the generalized forces were calculated without modification (see Table 2).

The deformations predicted by the EPCF model for symmetric loadings of the M=0,1 (Figure 10) and M=2,3 (Figure 11) 2D sponges are shown below; visually, they appear similar to the results obtained by Kushwaha $et\ al.$ using ANSYS APDL, most notably with the high stress regions occurring in the same locations.

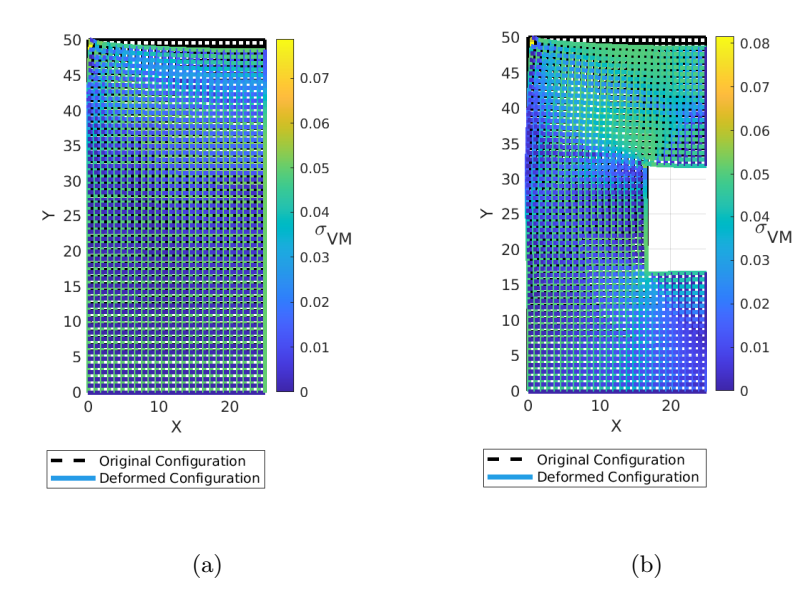


Fig. 10: Deformation of (a) M=0 and (b) M=1 Sierpinski Carpets under centrally-loaded compressive force using EPCF model with 2860 and 2774 frame elements, respectively. Displayed von Mises stresses are in MPa. (Compare deformations with result from ANSYS APDL with 2 million tetrahedral elements in Kushwaha *et al.* 2021⁴).

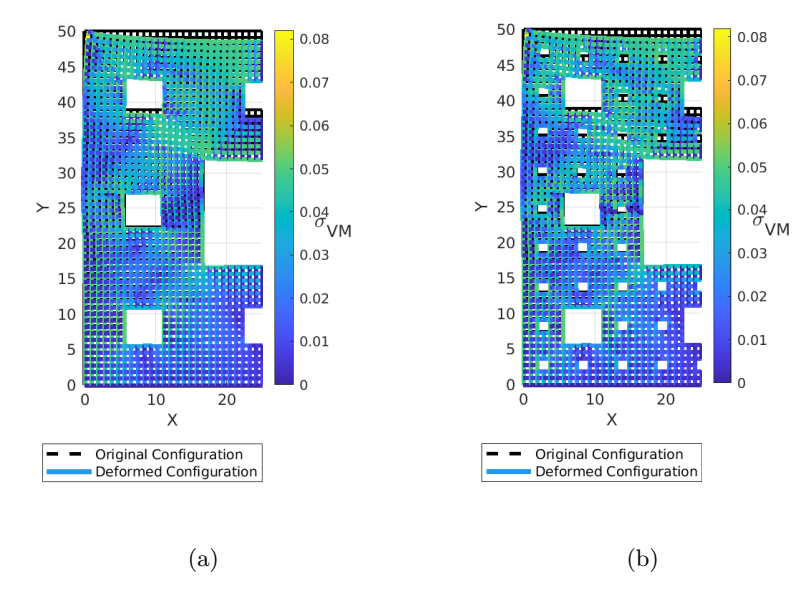


Fig. 11: Deformation of (a) M=2 and (b) M=3 Sierpinski Carpets under centrally-loaded compressive force using EPCF model with 2564 and 2496 frame elements, respectively. Displayed von Mises stresses are in MPa. (Compare deformations with result from ANSYS APDL with 2 million elements in Kushwaha etal. 2021^4).

Though the material they tested was non-metallic (PLA), we show in figure 12 that the EPCF model produces specific (density-normalized) compressive stress plateaus that seem reasonably consistent with the experimentally-predicted specific compressive stress values at small strains, replicating the behavior they describe (elastic loading region followed by a plateau in the compressive stress). In particular, Kushwaha et al. 2021⁴ state that "It can be concluded that there exist two distinctive compressive strain regimes for all the levels of the structure: 1) linear elastic region and 2) a plateau region". Figure 11 shows qualitatively similar behavior, in particular showing close matches of the plateau stress with much less computational resources and effort. To address the 2D reduction of the 3D model, the effective densities used to determine the specific stress are modified from the 3D values as 1.11, 0.988, and 0.7023 kg/m³ for the M = 1, 2, and 3 carpets, respectively (determined via subtracting empty portions from the 2D sponge and multiplying the resulting fractional value times the bulk density of 1.25 kg/m^3).

Only the plateau associated with the M=3 sponge disagrees strongly with the experimentally-predicted plateau, with the EPCF predicting a much higher compressive stress than observed; referring to the supplementary videos associated with Kushwaha et al., we see that, for the M=3 case, the thin geometry associated

with the numerous holes in the sponge lead to early buckling, a failure mode that is not accounted for in the small-deformation EPCF model, thus it is to be expected that the EPCF would anticipate higher stress before failure. Additionally, we note from the supplementary video that the initial loading does not appear to deform the structure much, and the initial strains recorded in the plot may be due only to cross-head movement.

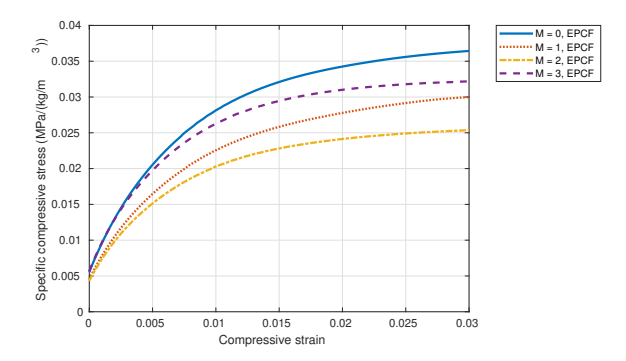


Fig. 12: Specific compressive stress (stress/density) results determined using elastic-plastic continuous-flow (EPCF) model 2D sponge simulations, for 3D printed PLA Menger sponge specimens of increasing Menger Sponge level; plateau values for $M = 0, 1, \text{ and } 2 \text{ compare favorably against Figure 1(c) in,}^4 \text{ but more detailed comparison is not possible due to the use of PLA, as no loading-unloading data was provided.}$

While using a 2D analogue of the Menger sponge can produce comparative results significantly faster, the EPCF model is, of course, suitable for use with 3D simulations also. Using a tessellation density that is consistent between the M=1,2, and 3 sponges (with the same density along the cross-section as that of the 2D Sierpinski carpet meshes), we performed a simulation of a compressive loading of three Menger sponges.

The locations of maximum von Mises stress predicted by the EPCF model compare favorably with those obtained in Kushwaha et al.⁴ as can be seen below in Figures 16 and 17. We should note that the location of the maximum stresses is probably the extent of the comparison possible in this case, since the result shown in Kushwaha⁴ is for larger deformation than would be accurate to simulate under the assumptions of the EPCF model. (Our maximum compressive strain is half that in their simulation, but as can be seen in Figure 12, the plateau stress is still approached, even at this reduced strain input.) Additionally, uncertainty about the form of the loading boundary conditions used in their ANSYS simulation likely influences any discrepancy between the results.

With the ability to predict elastic-plastic deformations in complex structures but at greatly-reduced effort from both the engineer and the computer, the simu-

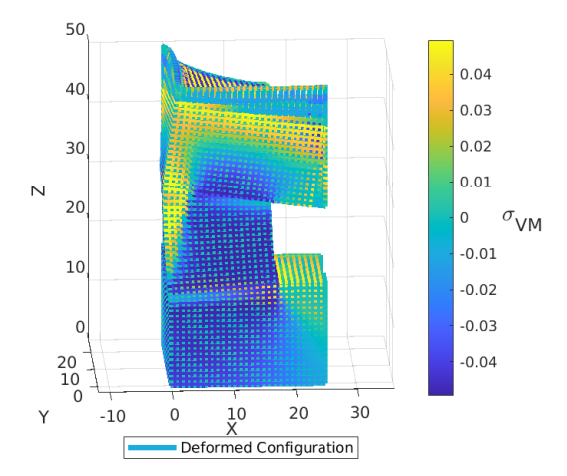


Fig. 13: Deformation of M=1 Menger Sponge under centrally-loaded compression using EPCF model with 94734 frame elements. Displayed von Mises stresses are in MPa. Pictured deformations are scaled by a factor of 5 for visibility.

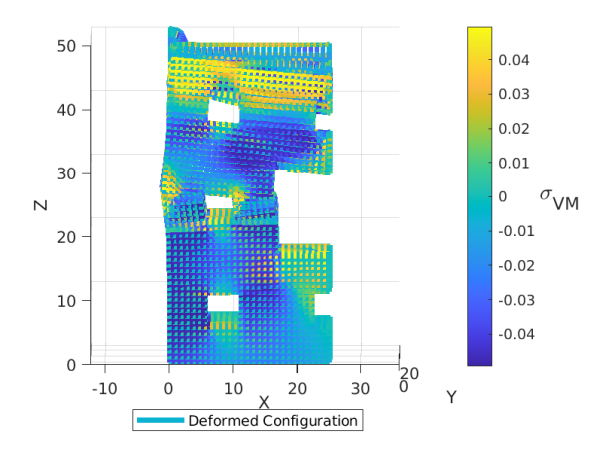


Fig. 14: Deformation of M=2 Menger Sponge under centrally-loaded compression using EPCF model with 74976 frame elements. Displayed von Mises stresses are in MPa. Pictured deformations are scaled by a factor of 5 for visibility.

lation of lengthy cyclic histories for this kind of structure is in reach. Though large deformations are not suitable for use with the EPCF model as described in this work, we are not interested in those for the purposes of fatigue analysis. (With this limitation in mind, care must be taken when using this model to avoid cases in

26 D. Jarecki et al. 2023

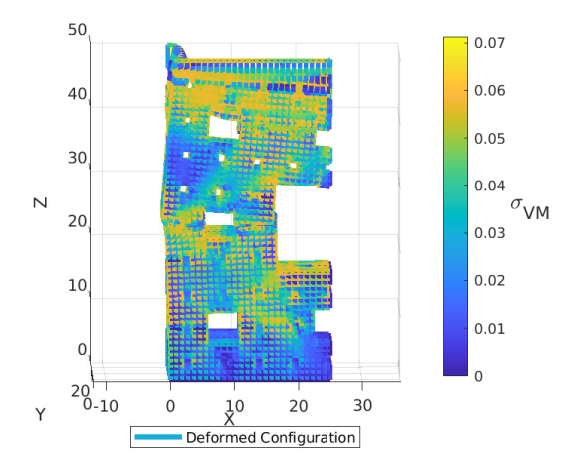


Fig. 15: Deformation of M=3 Menger Sponge under centrally-loaded compression using EPCF model with 65572 frame elements. Displayed von Mises stresses are in MPa. Pictured deformations are scaled by a factor of 5 for visibility.

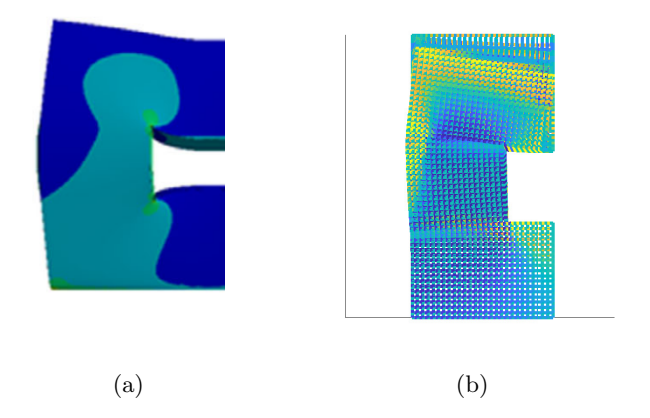


Fig. 16: Comparison of (b) EPCF deformation (scaled by a factor of 5) predictions with (a) fully-deformed result from ANSYS APDL with 2 million elements in Kushwaha $et\ al.\ 2021^4$) for M=1 Menger sponge. Note that the ANSYS model has much larger strains at its final state (large deformation model), so the stresses shown should not be identical.

which, even though macroscopic strains are small, locally large strains would be produced.)

The next sub-section demonstrates how the physically-based AMW fatigue parameter can be used with this model to predict fatigue without addition of a significant computational penalty (as compared to commonly-used methods such as

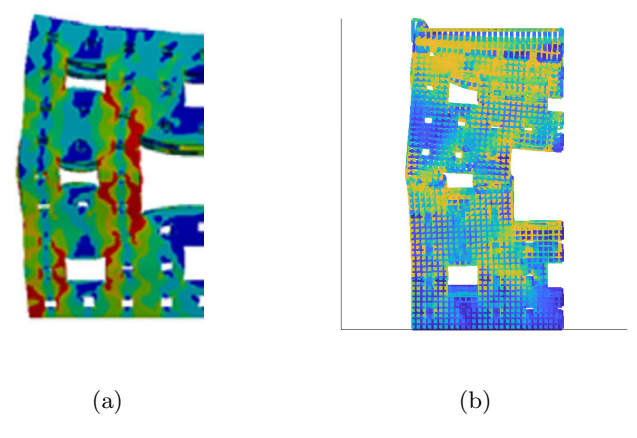


Fig. 17: Comparison of (b) EPCF deformation (scaled by a factor of 5) predictions with (a) fully-deformed result from ANSYS APDL with 2 million elements in Kushwaha et al. 2021^4) for M=3 Menger sponge. Despite the different colormapping scheme selected, it is evident that peak stresses are predicted in the same location for each model.

cycle counts, for which determination of the elastic-plastic history is only the beginning of the fatigue analysis). This can in turn be used to leverage the structural calculation capabilities demonstrated here.

4.5. Application to Physically-Based Fatigue Predictions

Dogbone specimens of various standardized shapes are used to replicate the stress states that appear in objects of engineering importance in the controlled environment of the laboratory. Direct simulation of the nonlinear, elastic-plastic stressstrain state that occurs in the body during deformation is, traditionally, quite computationally expensive, and requires careful meshing.

A recent work by Mozafari et al.³⁶ demonstrates the performance of the smoothyielding model combined with the accumulated microplastic work (AMW) fatigue parameter by predicting the fatigue life associated with multiple dogbone specimens. As can be seen in Figure 12 of, 36 defining the geometry accurately requires quite a few elements (612, 1545, and 5604, for the cases shown); we are able to produce comparable fatigue predictions with only 8 elements.

We reference the extensive Al 7075-T651 experimental results provided in Zhao and Jiang's excellent 2008 paper; 46 as described in detail in this work, multiple specimen types were used to perform tension, torsion, and tension-torsion tests. Using the specimen geometry taken together with the material parameters $(E = 0.717e5MPa, \nu = 0.306, YS = 501MPa)$, we determine the section moduli and the parameters that relate generalized load and yield (i.e., the μ -parameters). As an initial guess for the accumulated microplastic work at failure, we use the value

Table 3: List of section moduli used for Al 7075-T651 fatigue predictions, with the relevant specimen (and experimental runs from Zhao and Jiang 2008) noted.

Specimen	EA (kN)	$EI (\mathrm{kN/mm})$	GJ (kN/mm)
Solid Cylinder (2a)	7.68e6	6.55e7	5.02e7
Tubular (4a), (5c)-(5f)	9.91e6	6.05e8	4.63e8

Table 4: List of flow potential parameters used for Al 7075-T651 fatigue predictions, with the relevant specimen (and experimental runs from Zhao and Jiang 2008) noted.

Specimen	$\mu_n(\text{mm}^{-2})$	$\mu_y (\mathrm{mm}^{-3})$	$\mu_x(\text{mm}^{-3})$
Solid Cylinder (2a)	0.00933	0.00376	0.00415
Tubular (4a), (5c)-(5f)	0.00723	0.00103	0.00113

reported by Mozafari $et~al.^{36}$ for Al 7075- $T6~(\eta_f=2850{\rm MJ/}m^3)$ as the fatigue failure criterion, recognizing that the difference in material processing (and, potentially, surface finish) may require adjustments to the actual eta_f value that would be appropriate for use.

The complete structural parameters used by the EPCF model for this effort are reported in Tables 3 and 4. As noted in previous sub-sections, the smoothness parameter, α , associated with the EPCF beam element under pure torsion, pure bending, and pure axial deformation, is distinct. Using nonlinear FEA simulations with perfect plasticity as a baseline, however, would result in a continuous-flow parameter α parameter that is too large to accurately accrue fatigue damage from accumulated microplastic work. Referencing Mozafari et al.³⁶-in which the ξ value ($\approx 1/\alpha$) is determined to be 107 MPa for the case of Al-7075 T6-we select values near the inverse of their value for both tension and torsion, in particular, $\alpha_n = 8e - 3\text{MPa}^{-1}$ (for tension), and $\alpha_x = 10e - 3\text{MPa}^{-1}$ (for torsion).

Multiple strain control loading paths (including proportional, exactly 90° out-of-phase, and two out-of-phase Lissajous curves) are described in Figure 4 of Zhao and Jiang $2008;^{46}$ it is easy to convert these into load paths in displacement. We use the various displacement load paths as control input for an EPCF simulation set up as follows:

- Half of the specimen midsection geometry (from x = L/2 to x = L, where L depends on the particular specimen) was simulated;
- 8 nodes were used to discretize the length of the geometry into frame elements (following appropriate convergence analysis);
- Symmetry was enforced on one end (x = L/2); it was treated as fixed relative to the end under displacement control;
- Displacement was prescribed on the other end (x = L), according to the ap-

propriate waveforms for tension and torsion channels provided in Zhao and Jiang. 46

The EPCF simulations performed against the fatigue data collected in Table $2(a)^{46}$ were fully-reversed axial tension; Table $4(a)^{46}$ contained data from fatigue experiments performed in fully-reversed torsion. Table $5(d)^{46}$ contained data collected under 90° out-of-phase loading, and Tables 5(d) and $5(e)^{46}$ contained loading paths defined by Lissajous curves. No functional definition was provided for the Lissajous curves, but we fit the curves shown as follows; for 5(e), we specified axial channel u_{in} and shear channel ϕ_{in} as:

$$u_{in} = \frac{\Delta u_{in}}{2} \sin(t)$$
$$\phi_{in} = \frac{\Delta \phi_{in}}{2} \sin\left(2(8\pi)t - \frac{\pi}{1.9}\right)$$

where and for 5(f):

$$u_{in} = \frac{\Delta u_{in}}{2} \sin(t)$$
$$\phi_{in} = \frac{\Delta \phi_{in}}{2} \sin\left(4(8\pi)t - \frac{\pi}{2.3}\right)$$

where $\Delta u_{in}/2$ and $\Delta \phi_{in}/2$ denote the amplitudes for the prescribed displacements. Using these load paths, we are able to replicate the fatigue predictions under tension and tension-torsion with high accuracy, for most points staying within a factor of 2 (see Figure 18), with only the 90° out-of-phase results (circular, EPCF, 5d in Figure 18) presenting an issue.

Experimental results were taken from Tables 2, 4, and 5 in, ⁴⁶ omitting—for this work—nonzero mean cases. Future modification to the EPCF model to include kinematic hardening should allow general cyclic cases to be accurately handled.

5. Conclusion

This work demonstrates that a moment-curvature-based EPCF frame model can provide full-structural plasticity calculations in a computationally-efficient and accurate manner, replicating results obtainable by 3D FEA but with significantly lower degrees of freedom and greatly-reduced meshing efforts, particularly for complex micro-structures.

THis makes it possible to carry out cycle-count-free fatigue calculations via use of the accumulated microplastic work, something which classical J2 plasticity models (even with frame elements) available in commercial software are not capable of. This exciting development brings full-structural, time-domain fatigue calculations closer to the hands of the design engineer.

However the current approach has very simple cross sectional kinematics—the CS rotates rigidly. This is unrealistic and results in early plasticity (due to stiffer elastic response). The results can be further improved by considering cross sectional

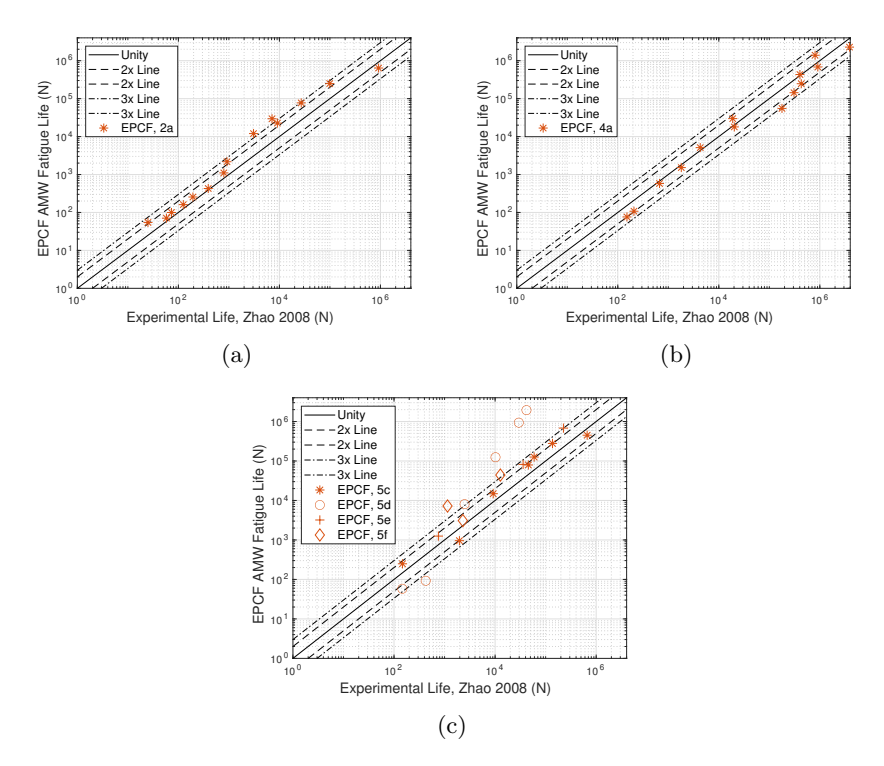


Fig. 18: Fatigue predictions produced by EPCF compared to experimental results of Zhao and Jiang:⁴⁶ (a) under tension, with zero mean stress (fatigue data from Table 2a); (b) under torsion with zero static axial load. Fatigue data taken from table 4a; and (c) Under Tension torsion with 4 different loading paths (fatigue data from table 5c-f in Zhao and Jiang⁴⁶)

warping (such as by using an approach similar to that developed by Payette and Reddy⁴⁷).

6. Acknowledgements

A. R. Srinivasa and Dominic Jarecki gratefully acknowledge the support of TDA, Inc. in conducting this research. J. N. Reddy and A. R. Srinivasa would also like to acknowledge National Science Foundation CMMI grant No. 1952873 for their support in the performance of this work. The authors are pleased to acknowledge the discussions with Dr. Archana Arbind (Indian Institute of Technology, Kharagpur, India) for some aspects of the formulation. The paper is dedicated to Professor Yeong-Bin Yang on his 70th birthday. Professor Yang's research and professional leadership has enormously benefited the structural mechanics community all over the world, and we wish him good health and happiness in the years to come.

References

- 1. M. Zhao, H. Qing, Y. Wang, J. Liang, M. Zhao, Y. Geng, J. Liang and B. Lu, Superelastic behaviors of additively manufactured porous niti shape memory alloys designed with menger sponge-like fractal structures, Materials & Design 200 (2021) p. 109448.
- 2. X. Zhang, F. Yang, B. Liu and J. Deng, Design of menger sponge fractal structural niti as bone implants, Modelling and Simulation in Materials Science and Engineering **29**(8) (2021) p. 084001.
- 3. N. Viet, N. Karathanasopoulos and W. Zaki, Effective stiffness, wave propagation, and yield surface attributes of menger sponge-like pre-fractal topologies, International Journal of Mechanical Sciences 227 (2022) p. 107447.
- 4. B. Kushwaha, K. Dwivedi, R. S. Ambekar, V. Pal, D. P. Jena, D. R. Mahapatra and C. S. Tiwary, Mechanical and acoustic behavior of 3d-printed hierarchical mathematical fractal menger sponge, Advanced Engineering Materials 23(4) (2021) p. 2001471.
- D. W. White, Plastic-hinge methods for advanced analysis of steel frames, Journal of Constructional Steel Research 24(2) (1993) 121–152.
- 6. O. Bayrak and S. A. Sheikh, Plastic hinge analysis, Journal of Structural Engineering, ASCE **127**(9) (2001) 1092–1100.
- 7. J. Y. R. Liew, H. Chen, N. E. Shanmugam and W. F. Chen, Improved nonlinear plastic hinge analysis of space frame structures, Engineering Structures 22(10) (2000) 1324 - 1338.
- 8. M. H. Scott and G. L. Fenves, Plastic hinge integration methods for force-based beamcolumn elements, Journal of Structural Engineering, ASCE 132(2) (2006) 244–252.
- G. Cocchetti and G. Maier, Elastic-plastic and limit-state analyses of frames with softening plastic-hinge models by mathematical programming, International Journal of Solids and Structures **40**(25) (2003) 7219–7244.
- 10. D. Ehrlich and F. Armero, Finite element methods for the analysis of softening plastic hinges in beams and frames, Computational Mechanics 35(4) (2005) 237–264.
- 11. M. Tabatabaei and S. N. Atluri, Simple and efficient analyses of micro-architected cellular elastic-plastic materials with tubular members, International Journal of Plasticity **99** (2017) 186–220.
- 12. N. Challamel, Dynamic analysis of elastoplastic shakedown of structures, International Journal of Structural Stability and Dynamics 5(02) (2005) 259–278.
- 13. P. M. Pimenta and T. Yojo, Geometrically exact analysis of spatial frames, Applied Mechanics Reviews **46**(11) (1993).
- 14. J. C. Simo and J. Kennedy, On a stress resultant geometrically exact shell model. part v. nonlinear plasticity: formulation and integration algorithms, Computer Methods in Applied Mechanics and Engineering 96(2) (1992) 133–171.
- 15. M. Saje, I. Planinc, G. Turk and B. Vratanar, A kinematically exact finite element formulation of planar elastic-plastic frames, Computer Methods in Applied Mechanics and Engineering 144(1-2) (1997) 125–151.
- 16. M. Saje, G. Turk, A. Kalagasidu and B. Vratanar, A kinematically exact finite element formulation of elastic-plastic curved beams, Computers & Structures 67(4) (1998) 197-214.
- 17. D. Zupan and M. Saje, Finite-element formulation of geometrically exact threedimensional beam theories based on interpolation of strain measures, Computer Methods in Applied Mechanics and Engineering 192(49-50) (2003) 5209-5248.
- L. Herrnböck, A. Kumar and P. Steinmann, Geometrically exact elastoplastic rods: determination of yield surface in terms of stress resultants, Computational Mechanics **67**(3) (2021) 723–742.
- 19. O. Weeger, D. Schillinger and R. Müller, Mixed isogeometric collocation for geometri-

- cally exact 3d beams with elasto-visco-plastic material behavior and softening effects, Computer Methods in Applied Mechanics and Engineering 399 (2022) p. 115456.
- 20. ASTM, E1049-85-Standard practices for cycle counting in fatigue analysis (2017).
- A. Ince and G. Glinka, A numerical method for elasto-plastic notch-root stress strain analysis, The Journal of Strain Analysis for Engineering Design 48(4) (2013) 229–244.
- 22. A. Ince, G. Glinka and A. Buczynski, Computational modeling of multiaxial elastoplastic stress–strain response for notched components under non-proportional loading, *International Journal of Fatigue* **62** (2014) 42–52.
- A. Ince and G. Glinka, Innovative computational modeling of multiaxial fatigue analysis for notched components, *International Journal of Fatigue* 82 (2016) 134–145.
- Y. Garud, Prediction of Stress-Strain Response under General Multiaxial Loading (ASTM International, 1982).
- Y. Jiang and H. Sehitoglu, Modeling of cyclic ratchetting plasticity, part i: Development of constitutive relations, *Journal of Applied Mechanics, Transactions ASME* 63(3) (1996) 720–725.
- 26. Y. Jiang and H. Sehitoglu, Modeling of cyclic ratchetting plasticity, part ii: Comparison of model simulations with experiments, *Journal of Applied Mechanics, Transactions ASME* **63**(3) (1996) 726–733.
- Y. Jiang and J. Zhang, Benchmark experiments and characteristic cyclic plasticity deformation, *International Journal of Plasticity* 24(9) (2008) 1481–1515.
- 28. D. Benasciutti and R. Tovo, Cycle distribution and fatigue damage assessment in broad-band non-gaussian random processes, *Probabilistic Engineering Mechanics* **20**(2) (2005) 115–127.
- T. Dirlik and D. Benasciutti, Dirlik and tovo-benasciutti spectral methods in vibration fatigue: a review with a historical perspective, Metals 11(9) (2021) p. 1333.
- 30. M. Bonte, A. de Boer and R. Liebregts, Determining the von mises stress power spectral density for frequency domain fatigue analysis including out-of-phase stress components, *Journal of Sound and Vibration* 302(1-2) (2007) 379–386.
- 31. D. Jarecki, A. R. Srinivasa, N. Iyyer and P. Thamburaja, Spectral fatigue prediction with a unified strain-based approach to handle localized plastic excursions, *Mechanical Systems and And Signal Processing* **Under Review** (2023).
- 32. K. R. Rajagopal and A. R. Srinivasa, Inelastic response of solids described by implicit constitutive relations with nonlinear small strain elastic response, *International Journal of Plasticity* **71** (2015) 1–9.
- 33. Z. Wang, A. R. Srinivasa, K. R. Rajagopal and J. N. Reddy, Simulation of inextensible elasto-plastic beams based on an implicit rate type model, *International Journal of Non-Linear Mechanics* **99** (2018) 165–172.
- 34. F. Mozafari, P. Thamburaja, A. R. Srinivasa and N. Moslemi, A rate independent inelasticity model with smooth transition for unifying low-cycle to high-cycle fatigue life prediction, *International Journal of Mechanical Sciences* 159 (2019) 325–335.
- F. Mozafari, P. Thamburaja, A. R. Srinivasa and S. Abdullah, Fatigue life prediction under variable amplitude loading using a microplasticity-based constitutive model, International Journal of Fatigue 134(November 2019) (2020) p. 105477.
- 36. F. Mozafari, P. Thamburaja, N. Moslemi and A. R. Srinivasa, Finite-element simulation of multi-axial fatigue loading in metals based on a novel experimentally-validated microplastic hysteresis-tracking method, Finite Elements in Analysis and Design 187 (2021) p. 103481.
- 37. D. Jarecki, A. R. Srinivasa and N. Iyyer, Rate-independent elasto-plastic materials—a brief history and some new developments, *International Journal of Advances in En-*

- gineering Sciences and Applied Mathematics 13(1) (2021) 3-17.
- 38. W. J. Stronge and T. Yu, Dynamic Models for Structural Plasticity (Springer, 1993).
- 39. M. Bruneau, C.-M. Uang and R. Sabelli, Ductile Design of Steel Structures (McGraw-Hill Education, 2011).
- 40. R. G. Budynas and A. M. Sadegh, Roark's Formulas for Stress and Strain (McGraw-Hill Education, 2020).
- 41. F. Mollica and A. R. Srinivasa, A general framework for generating convex yield surfaces for anisotropic metals, $Acta\ Mechanica\ {\bf 154} (1)\ (2002)\ 61–84.$
- 42. J. N. Reddy, Introduction to the finite element method (McGraw-Hill Education, 2019).
- 43. J. C. Simo, Algorithms for static and dynamic multiplicative plasticity that preserve the classical return mapping schemes of the infinitesimal theory, Computer Methods in Applied Mechanics and Engineering 99(1) (1992) 61–112.
- 44. N. A. Kazerooni, A. Srinivasa and A. Freed, Orthotropic-equivalent strain measures and their application to the elastic response of porcine skin, Mechanics Research Communications **101** (2019) p. 103404.
- 45. A. D. Freed and K. Rajagopal, A promising approach for modeling biological fibers, Acta Mechanica 227 (2016) 1609–1619.
- 46. T. Zhao and Y. Jiang, Fatigue of 7075-t651 aluminum alloy, International Journal of Fatigue **30**(5) (2008) 834–849.
- 47. G. Payette and J. Reddy, A nonlinear finite element framework for viscoelastic beams based on the high-order reddy beam theory, Journal of engineering materials and technology 135(1) (2013) p. 011005.